

# Mechanical Behavior of Steel and Aluminum Foams at Elevated Temperatures. Local buckling based approach toward understanding of the material system behavior

M. Tavares<sup>a</sup>, J. M. Weigand<sup>b</sup>, L. C. M. Vieira Jr.<sup>a</sup>, S. J. C. Almeida<sup>a</sup>, S. Szyniszewski<sup>c,\*</sup>

<sup>a</sup>*Department of Structural Engineering, State University of Campinas, Campinas, Brazil*

<sup>b</sup>*National Institute of Standards and Technology (NIST), Gaithersburg, Maryland, USA*

<sup>c</sup>*Department of Engineering, Durham University, Durham, UK*

---

## Abstract

The objective of this study is to understand and quantify the thermo-mechanical behavior of hollow sphere (HS) steel and powder metallurgy (PM) aluminum foams over a broad range of elevated temperatures. The behavior of both the HS steel and PM aluminum foam is tested under compressive loading at ambient temperature (24 °C) and elevated temperatures of 100 °C, 150 °C, 200 °C, 300 °C, 400 °C, 550 °C and 700 °C, and results for the two foams are compared by their rates of degradation in mechanical properties. To link the cell geometry and base metal properties with the global mechanical performance, the experimental work is underpinned by a computational micro-model, consisting of an assembly of hollow spheres. The computational model shows that plastic buckling of cells with progressive plasticity of the contact area is the key local failure mechanism. As expected, due to the plastic buckling of the unit cells, thermal degradations of the tested metallic foams follow similar trends as does the yield stress of their bulk metals. The HS steel foam exhibits only minor elevated-temperature-induced degradation in stiffness and strength at or below 400 °C, while still maintaining 69 % of its compressive strength at 550 °C. Comparatively, the PM aluminum foam begins degrading at an elevated temper-

---

\*Corresponding author

Email address: [s.szyniszewski@gmail.com](mailto:s.szyniszewski@gmail.com) (S. Szyniszewski)

ature of only 150 °C. Interestingly, the HS steel foam oxidized between 300 °C and 400 °C, resulting in corresponding increases in the quasi-elastic modulus of elasticity. Future work might explore how to take advantage of oxidation reactions at the surfaces of the cells in the design of components using HS steel foams. Our computational study also revealed a possible new regime of cellular structures made up of ultra-thin-walled spherical cells that are predicted to fall within the elastic buckling regime at the local level. Thus, their deformations would be reversible even under high strains and their thermal behavior would be only controlled by thermal deterioration in the elastic constants, rather than plasticity parameters such as the yield stress.

*Keywords:* Metallic foam, Plastic buckling, Thermal analysis, Hollow-sphere steel foam, Thermo-mechanical analysis, Fire.

---

## 1. Introduction

Cellular materials are commonly found in nature (for example, bird bones, cork) because they are lightweight, and tissue can grow into their open cells enhancing biological interfaces. Metallic foam is an intentionally porous metal substratum largely made up of voids varying in size from nanometers to millimeters. Because the physical parameters of a metal foam, such as its porosity, can be readily controlled during manufacture, the metallic foam's modulus of elasticity and yield stress can be tuned to satisfy an engineering project's specific needs, especially in the context of multi-functional and multi-physical engineering applications.<sup>10</sup>

Metallic foams have inherent fire retardancy, low thermal conductivity (relative to traditional metal structural components), and acoustic shielding. Open cell foams, albeit more expensive than conventional materials, also provide air, vapor, and fluid transport capabilities. Open cell foams act efficiently as heat exchangers due to the turbulent well-mixing flow that occurs within the foam's irregular micro-structural cavities, combined with the large surface area of their pores and high thermal conductivity of their base metals. The influences of

various micro-structural properties of metal foams, such as their porosity, pore and fiber diameters, tortuosity, pore density, and relative density on the heat  
20 exchanger performance were discussed in [? ]. Vadawala [? ] showed that a new composite material combining copper foam with wax was efficient in increasing the thermal conductivity of thermal energy storage systems. Cellular metals are also used as catalyst support in fuel cells. Their large surface area and mixing potential increases the intensity of the interaction between the catalyst  
25 and the fluid medium. Yuneta et al. [? ] provides a review of the fabrication, characterization, and application of porous metal materials to fuel cells.

While existing applications for metallic foams reside largely in the mechanical, aerospace, and automotive domains [? ], decreasing manufacturing costs and more widespread adoption of full-scale production techniques has ushered  
30 in the potential for using metallic foams in civil infrastructure applications. Metallic foams exhibit excellent stiffness-to-weight ratios, in comparison to conventional building materials, under a variety of loading conditions. For example, Banhart and Seeliger [? ] showed that foam panels have higher bending stiffness than solid steel sheets of the same weight. Metallic foams are also renowned for  
35 their compressibility because they can reliably sustain 90 % engineering strain prior to failure [? ], lending them extraordinary energy dissipation capacity [? ]. Energy dissipation via large compressive deformations at low-amplitude stress levels has been explored by the automotive industry as a potential crash protection technology [? ].

40 The ambient-temperature mechanical properties of metallic foams, specifically steel and aluminum foams, are characteristically different from those of their solid base metals. Steel foam is highly-compressible after yielding, unlike solid steel [? ], which exhibits only shear deformations and is incompressible in the plastic regime. Also, foams tend to fracture under tensile strains that are  
45 noticeably lower than their crushing and compaction strains [? ] thus warranting tailored respective failure criterions. Szyniszewski et al. [? ] tested fifty hollow sphere (HS) steel foam bars to measure their compressive yield stress, densification strain, compressive plastic Poisson's ratio, compressive unloading

modulus, as well as axial and shear mechanical properties at ambient temperature. Szymiszewski et al. [? ] noted the importance of correctly assessing Poisson's ratio due to its link to foam compressibility as shown by Deshpande and Fleck [? ].

Research has shown that temperature influences the mechanical properties of engineering materials [? ], and can reduce capacity of engineering systems such as sandwich panels [? ]. Thermo-mechanical behavior is also important for manufacturing approaches employing electrical current or electromagnetic forming (EMF) [? ]. Elevated temperatures have a significant influence on the compressive behavior of metallic foams. [? ] conducted a series of compressive tests on ALPORAS, a commercially-available closed cell aluminum foam manufactured by the Shinko-wire Company, at temperatures ranging from 25 °C to 620 °C. They found that the foam's compressive strength decreased both with decreased density and increased temperature. [? ] tested the mechanical properties of powder metallurgy steel foams at ambient and elevated temperatures, and reported an increase in compressive yield strength and stiffness for temperatures at or below 400 °C, and a decrease in compressive yield strength and stiffness above that temperature. [? ] concluded that the aging effect (i.e., dynamic age-hardening) was responsible for the increase in mechanical properties up to 400 °C. [? ] examined the high-temperature compressive behavior of powder metallurgy aluminum foams at temperatures ranging from 20 °C to 500 °C. They observed that increased temperatures resulted in decreased compressive strength and decreased energy absorption capacity, but increased densification strain (i.e., plateau length) at constant density. [? ] also reported that exposure time (the amount of time which the specimen was held at a constant elevated temperature before compressing it) did not influence the foam's compressive behavior. As part of a broader study on the behavior of ex-situ aluminum-alloy filled tubes under elevated temperatures (see [? ]), [? ] performed one quasi-static compressive test of a closed-cell aluminum foam specimen at temperatures of 25 °C, 150 °C, 300 °C, and 450 °C. Their results found only minor degradation in yield stress at or below 300 °C, after which, be-

80 cause of passing through its transition temperature, the degradation was more pronounced. [?] notes that, as the aluminum cell-walls began softening at higher temperatures, the morphology of the compressive stress-strain behavior became smoother, such that the aluminum foam behaved in a similar manner as a ductile metal.

85 Many additional studies have investigated the compressive behavior of composite or alloyed metallic foams at elevated temperatures. After testing the compressive behavior of cenosphere-filled aluminum syntactic foams at elevated temperatures of 100 °C and 200 °C, and strain rates ranging from  $10^{-3}/\text{s}$  to  $1/\text{s}$ , [?] found that plateau stress decreased with temperature irrespective of  
90 strain-rate. [?] tested Distaloy (Cu-Ni-Mo) and Astaloy (Mo) foams having different degrees of porosity at elevated temperatures of 200 °C, 400 °C, and 600 °C. They found that the length of the yield plateau (in units of compressive strain) was appreciably affected by porosity but not temperature. They also observed that compressive yield strength increased up to a temperature of 400 °C,  
95 after which it sharply decreased at 600 °C. [?] investigated the compressive behavior of composite Al-Si-SiC foams at elevated temperatures, evaluating the influence of temperature on energy absorption and type of fracture. They reported a decrease in compressive strength with increasing temperature, as well as a decrease in absorbed energy when a ductile-type fracture mode occurred.  
100 [?] tested expanded perlite-aluminum syntactic foam cylinders in compression at elevated temperatures, comparing the foam's resulting temperature-degraded mechanical properties against those of the matrix materials, tested under the same conditions. Their results showed that the high-temperature behavior of the foams was controlled both by temperature-dependent softening of the matrix materials and a transition of the deformation behavior of the foam from brittle at low temperatures to ductile at high temperatures. [?] investigated the effect of temperature on the microstructure, failure mechanism, and compressive mechanical properties of commercially-available zinc-aluminum alloy syntactic foams with expanded perlite or expanded glass filler particles at four elevated  
105 temperatures of 100 °C, 200 °C, 300 °C, and 350 °C. The results showed that  
110

while the foam with expanded perlite was stronger than the foam with expanded glass across all elevated temperatures, the relative reduction of plateau stress of the two foams was similar.

As a continuation of the work presented in [? ], this study examines the thermo-mechanical behavior of HS steel foam samples removed from the same rectangular prism. Specifically, this paper characterizes and compares the mechanical properties of HS steel and powder-metallurgy (PM) aluminum foam specimens both exposed to a wide range of elevated temperatures, up to 700 °C and 500 °C, respectively, for durations of 15 min and 30 min. Consistent with ISO Standard 13314:2011, the yield strength and plateau stress are calculated for each specimen. To permit additional characteristics of their compressive stress-strain responses to be calculated, for example the strain at which densification begins, a nine-parameter phenomenological equation fitted to the compressive stress-strain response of each specimen. Finally, to examine the plasticity that localized at sphere interfaces due to contact forces, high-fidelity computational models of hollow-sphere foams were also conducted using LS-DYNA [? ].

## 2. Experimental approach

### *Material samples*

A HS steel foam rectangular prism, sourced from Fraunhofer Institute in Germany, with dimensions of 22 cm × 5.2 cm × 5.2 cm, was cut and machined into 10 cylindrical specimens following the specifications in the ISO Standard 13314:2011 [? ]. The cylindrical specimens had a diameter of 25 mm and length of 50 mm (Figure 1).

According to ISO standard for testing, all spatial dimensions of the specimen shall be at least 10 times larger than the average pore size and no less than 10 mm, and the ratio of the length to the diameter shall be between 1.0 and 2.0. The measured average pore size was 2.27 mm, and the method for determining the average pore size is explained below. Between 12 and 14 spheres typically spanned across the 25 mm radius. The specimens had an average 85 % porosity,

<sup>140</sup> calculated based on the dimensions and volume of the specimens. The base metal was mild steel with 0.3 % to 0.5 % carbon content and 0.5 % phosphorous content. Based on that chemical composition, the base metal's bulk yield stress was estimated as 250 MPa, using the method outlined in [? ]. [? ] reported a yield stress of 260 MPa for the same material. The ultimate tensile capacity of <sup>145</sup> the base metals was estimated as 500 MPa, based on tests performed by IFAM on tensile specimens produced by Spark Plasma Sintering and homogenization annealing. This estimate was consistent with data for alloys with similar carbon and phosphorous contents reported in the literature, see Worldwide Guide to Equivalent Irons and Steels table with Australian steel [? ].

<sup>150</sup> The rectangular prism of PM aluminum foam had dimensions 14.8 cm × 6.0 cm × 6.0 cm, and was sourced from Fraunhofer Institute for Machine Tools and Forming Technology IWU in Chemnitz, Germany. Like for the HS steel specimens, the PM aluminum foam prism was machined into 8 cylindrical specimens, each with a diameter of 25 mm and length of 50 mm, in accordance with <sup>155</sup> ISO 13314:2011. Due to the inherent heterogeneity of PM foams, the porosity varied between 71.4 % and 81.8 % for the 8 cylindrical specimens. The base metal consisted of a common aluminum alloy AW-6060 (AlMgSi0.5).

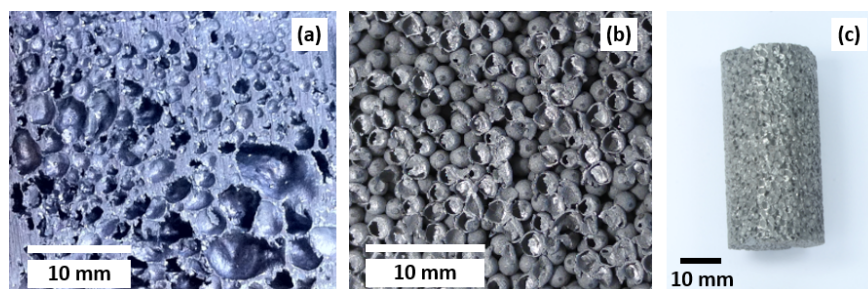


Figure 1: Metallic foam samples: (a) closeup view of PM aluminum foam, (b) closeup view of HS steel foam, and (c) HS steel foam cylinder specimen prior to compressive testing. The aluminum foam resembles a highly porous metallic medium while the steel foam resembles closely packed hollow spheres.

### Pore Size Dimensions

The dimensions of the pores were determined to ensure that each cross-section contained a sufficient number of pores to achieve relatively homogeneous material properties. Based on a high-definition image of a transverse cut of the base samples, the largest dimension of 242 pores for HS steel foams and 237 pores for aluminum foam were measured. The 20 mm distance between the jaws of a Mitutoyo digital caliper was used as a reference length for the pixel distance measurement. 726.20 pixels = 20 mm in the HS steel foam, and 236.51 pixels = 10 mm in the PM aluminum foam (see Figure 2).

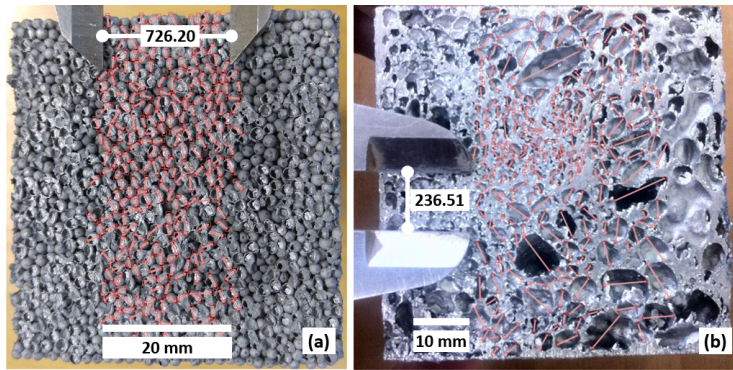


Figure 2: Method for measuring pore size for (a) HS steel foam specimens, and (b) PM aluminum foam specimens. Diameters of the spherical shells or pores are depicted using red lines.

A normal distribution with mean of 1.79 mm and variance of 0.19 mm<sup>2</sup> best described the pore sizes measured in the HS steel foam (Figure 3a). On the other hand, the aluminum foam's pore size was best captured by a lognormal distribution with mean of 2.13 mm and variance of 1.67 mm<sup>2</sup> (Figure 3b).

If the pore shape is spherical, the measurement of the pore size through a transverse cut will be smaller than the pore diameter, unless the cut passes exactly through the pore's center (Figure 4). Thus, an amplification factor was proposed to improve the estimate of the pore diameter from sectional pore measurements.

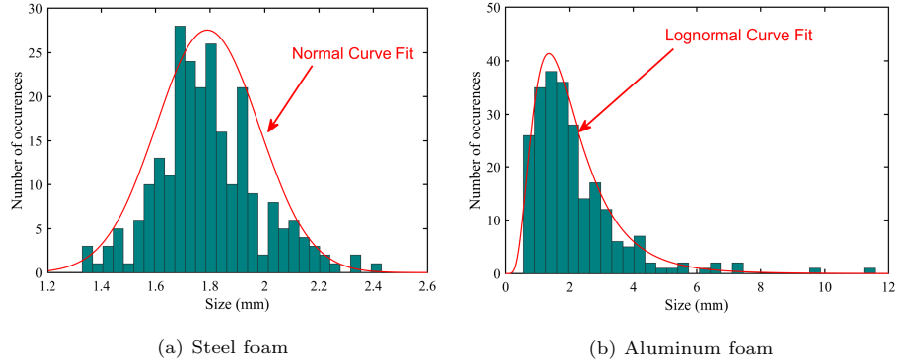


Figure 3: (a) Normal distribution of pore size of HS steel foam, (b) Lognormal distribution of pore size of PM aluminum foam. Independent of the distribution type, the HS steel foam had a lesser variability than did the PM aluminum foam, as characterized by a larger scatter in pore size.

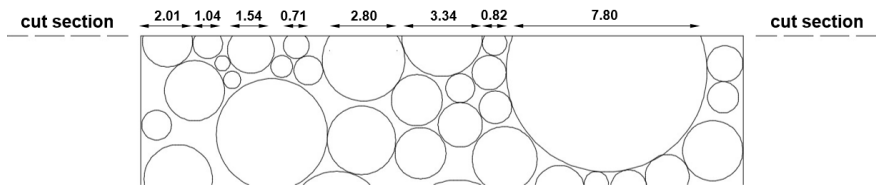


Figure 4: Schematic view of lateral cut plane through cylindrical sample. The cross-sectional diameters generally do not coincide with the true diameter of the sphere or cavity.

Let us consider an unknown amplification factor as the ratio between the mean of the projected radius values and the true sphere's radius (Figure 5). If all pores are assumed as spherical, random cuts can be generated using a uniform random distribution of  $h_{proj} \in \langle 0, r_{true} \rangle$  and for each cut a projected radius can be computed as:

180

$$r_{proj}^i = \sqrt{r_{true}^2 - h_{proj}^i} \quad (1)$$

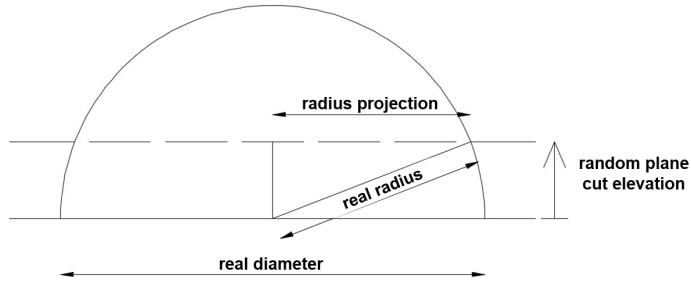


Figure 5: By cutting a sphere at a random elevation, the relationship between the expected mean radius in the cut plane and the real radius of the spherical cavity can be calculated.

Employing Monte-Carlo simulation, the average value of  $\hat{r}_{proj}$  was calculated; consequently, the correction factor was calculated as:

$$\alpha = \frac{r_{true}}{\hat{r}_{proj}} \quad (2)$$

185

An amplification factor  $\alpha = 1.27$  was obtained. This value resulted in corrected average pore diameters of  $1.27 \times 1.79 \text{ mm} = 2.27 \text{ mm}$  in HS steel foam and  $1.27 \times 2.13 \text{ mm} = 2.70 \text{ mm}$  for aluminum foam, which leads us to conclude that the specimens must have at least 22 mm and 27 mm of cross-sectional width respectively. Considering the size of aluminum and steel foam blocks, specimen 190 diameters of 25 mm were chosen as a representative for both base materials.

### **3. Behavior of HS steel and PM aluminum metallic foams at elevated temperatures**

#### *Mechanical testing*

Steel foam specimens were tested at 24 °C (ambient temperature), 150 °C,  
195 200 °C, 300 °C, 400 °C, 550 °C, and 700 °C, while aluminum foam specimens  
were tested at 24 °C, 150 °C, 200 °C, 300 °C, and 500 °C (Table 1). For the  
most part, two specimens were tested at each temperature except ambient; one  
exposed to the elevated test temperature for 15 min, and the other exposed  
for 30 min. The exceptions were the 550 °C and 700 °C tests on the HS steel  
200 foam, and the 500 °C test on aluminum foam, which were all exposed for only  
15 min. For each test, the high-temperature furnace was heated to the test  
temperature without the specimen inside. Once the targeted elevated tempera-  
ture was reached, the cylindrical metallic foam specimen was placed inside the  
furnace. The compressive test was not started until the specimen had reached  
205 and been held under a steady-state conditions at the target testing temperature  
for the required exposure time. The testing temperature was regulated by a  
thermocouple installed on the side of each specimen. [?] reported that mild  
steel melts at a temperature of approximately 1536 °C, and [?] estimated  
the aluminum melting temperature at approximately 660 °C. The majority  
210 of the testing temperatures was conducted at elevated temperatures less than  
400 °C because, based on both the available literature and EN 1993-1-2:2005 [?]  
], the strength of steel is severely degraded at elevated temperatures exceeding  
400 °C. The sensitivity of the mechanical properties to exposure time was eval-  
uated by conducting the compressive testing following both 15 min and 30 min  
215 of steady-state pre-heating.

#### *3.1. Testing approach*

The compressive testing was conducted using a servo-hydraulic Materials  
Testing Systems (MTS) Model 810 Universal Testing Machine (UTM), with a  
capacity of 100 kN in compression. A MTS Model 652.01 High-Temperature  
220 Electric Furnace applied the thermal loads (Figure 6).

Table 1: Temperature and exposure time during compressive experiments

Temperature (°C)	Steel Foam		Aluminum Foam	
	Melting point (%)	Duration (min)	Melting point (%)	Duration (min)
24	2	$\infty$	4	$\infty$
150	10	15 & 30	23	15 & 30
200	13	15 & 30	30	15 & 30
300	20	15 & 30	45	15 & 30
400	27	15 & 30	-	-
500	-	-	76	15
550	37	15	-	-
700	47	15	-	-

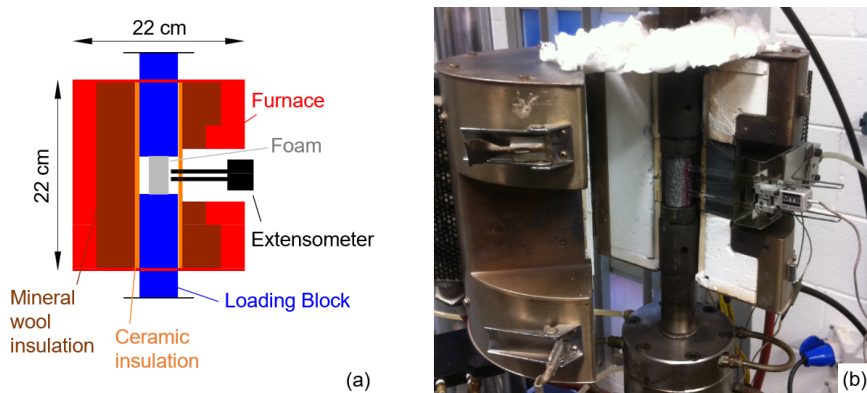


Figure 6: Experimental setup for thermal-mechanical compressive testing: (a) annotated schematic of high-temperature furnace, and (b) actual view of the opened furnace. Specimens were first heated and subsequently loaded in compression after internal temperature stabilized at target test temperature. Strains were measured using an extensometer placed inside the furnace.

Mechanical loads in the UTM were controlled using a MTS Flex Test 60 controller, and the furnace was controlled using a MTS Digital PID Temperature Controller. The high-temperature furnace allows pre-heating at temperatures up to 1000 °C, has multi-zone temperature control to compensate for vertical temperature gradients, and is accurate (at the constant steady-state temperature) to within  $\pm 2$  °C. After a preload of 0.10 kN was applied to remove any surface irregularities, axial loading was applied pseudo-statically using displacement control at a constant loading rate of 0.025 mm/s. The reported compressive stress,  $\sigma$ , was calculated as the ratio of the applied force  $F$  to the measured cross-sectional area before loading. Ideally, the reported compressive strain  $\epsilon$  would be measured using the available MTS High-Temperature Axial Extensometer. However, for many specimens the tips of the extensometer leads slipped at relatively low compressive loads, and thus for consistency the compressive strain was calculated as the ratio of crosshead displacement to the measured length of each undeformed cylindrical specimen.

### *3.2. Experimental stress-strain curves*

The compressive stress-strain behavior of metallic foams exhibited three distinct phases of behavior (Figure 7). Until yield, the behavior was elastic (Elastic Phase), and the stress was linearly related to the strain. After yield was a large plastic plateau (Plateau Phase). Within this region, an upper and lower yield point can be identified. The final phase (Densification Phase) is characterized by densification of the metallic foam, during which the stiffness of the compressive stress-strain curve rapidly increases. During densification, the cell walls of the metallic foam begin to buckle and contact one another as the voids close. The densification phase continues until the metallic foam reaches its compressibility limit. The slope of the stress-strain curve within the densification phase is defined as the densification modulus.

Results from the steel and aluminum foam specimens tested under uniaxial compression at elevated temperatures are shown in Figures 8a) and 8b), respectively. Similar trends were observed for both types of metallic foam, in that each

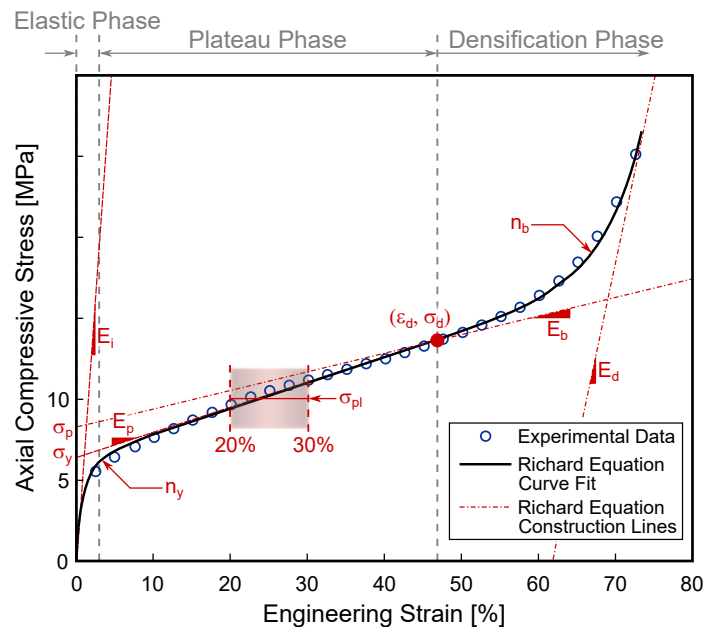


Figure 7: Three phases of compressive behavior of metal foams comprising an elastic phase, plateau phase, and densification phase. Plot annotations schematically depict the parametrization of the non-linear stress strain behavior of metallic foams, defined in Equation (11).

specimen exhibited, but to varying degrees, the three phases of behavior shown in Figure 7. The exposure (15 min or 30 min) did not appear to have had a systematic influence on the stress-strain behavior of the specimens. Kovacicetal [?] also reported that exposure time to elevated temperature did not influence  
255 the foam's compressive behavior.

An insightful reader might notice that properties at 300 °C are higher than room temperature or 100 °C. In addition, those from 400 °C are higher than those from 200 °C, which might initially seem puzzling. However, a thin blue oxide film was observed to form on all cells of the steel foam specimens at  
260 temperatures exceeding 250 °C (see Figure 9). The effect of steel oxidation at around 300 °C, the so-called “blue brittleness effect”, is a phenomenon that occurs in steel alloys with significant Carbon content upon heating, particularly within temperatures ranging from 180 °C to 370 °C ([? ]). The blue oxide layer, which forms on the surface of the metal, is stiffer and stronger than the base  
265 steel alloy but more brittle. The addition of a stiffer film on the cells increased the macroscopic stiffness of the foam due to the large surface area relatively to the volume of the base material. The effect of the distributed stiffening of the steel foam become negligible at higher temperatures when the base steel of the cells deteriorated past the transition temperature of 400 °C. The effect of  
270 a blue oxide film also affected parametric properties of the stress-strain curves, such as plateau stress in the systematic analysis of the macroscopic steel foam properties at elevated temperatures described later in the paper.

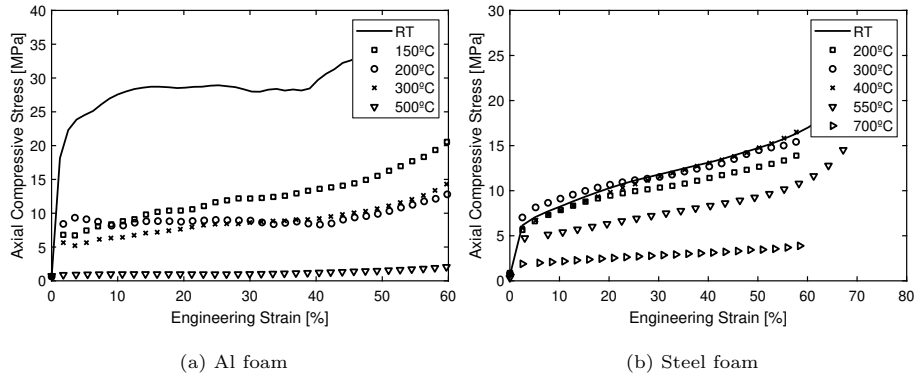


Figure 8: Stress-strain behavior of metallic foam specimens at ambient and elevated temperatures for (a) HS steel foam specimens, and (b) PM aluminum foam specimens.



Figure 9: (left) HS steel foam specimen before testing, and (right) HS steel foam specimen after testing at 300 °C following 30 min of exposure. Discoloration of the heated specimen indicated formation of a blue oxide film on the surfaces of the spherical shells.

#### 4. Micro-mechanical simulations

The microstructure of a sintered HS foam consists of hollow spheres and  
275 welds between those spheres. The spheres have been shown to be in a random close-packed (RCP) stacking configuration [? ]. Wouterse and Philipse [? ] tested five algorithms for generating random RCP sphere stacking and showed that two different variations of the “Mechanical Contraction Method” resulted in stackings that were most like an experimental stacking in their geometric  
280 properties. The algorithmically simpler of those two methods, the “Modified Mechanical Contraction Method”, was chosen for the presented simulations, which involves the steps below. These steps are described in more detail in [? ], [? ].

1. Randomly place spheres of zero size throughout the domain.
- 285 2. Increase the size of all spheres by an equal magnitude.
3. Check for overlapping spheres and move both spheres in each overlap pair away from each other by an equal magnitude. Repeat this step until all but a minimum threshold of overlaps are eliminated.
4. Repeat Steps 2 and 3 until the final sphere size is reached.

290 After the spheres are successfully placed, welds are inserted to connect them. The actual welds between the spheres are solid circular shapes with concave sides which curve until they reach a tangent with the sphere. However, due to the difficulty of modeling such a shape, these welds were approximated by a straight cylinder of a given diameter connecting any spheres within a specified threshold  
295 distance. The random variables in this geometry algorithm include sphere size, wall thickness, and sphere location. The deterministic variables include the weld size, structure, and some of the input parameters for the Modified Mechanical Contraction Method such as the number of spheres to initially place and the number of overlaps threshold at which to increment the size of the spheres.

300 The core algorithms and functionality of the simulator was originally developed by Smith and Arwade ([? ? ]). The algorithm produced geometries such

as that displayed in Figure 10a). The original implementation used the AD-INa solver, but in this study, the scripts were modified to generate meshes for LS-DYNA ([? ]) due to its superior ability to handle multiple, concurrent contacts. The analyses used an implicit integration scheme for numerical efficiency and stability. The mechanical properties of the base steel at ambient temperature and 550 °C as shown in Table 2. The properties are based on mechanical testing of samples with similar chemical content, namely Fe-C(0.5)-P(0.5) by Fraunhofer Institute in Dresden and independent data from World Wide Guide of Equivalent Irons and Steels ([? ]).  
 305  
 310

Table 2: Mechanical properties employed in the simulations.

Property	Value	
	Ambient	550 °C
Young modulus, GPa	200	91
Poisson ratio	0.29	0.29
Yield stress, MPa	250	67.5
Ultimate strain, mm/mm	0.18	0.21
Ultimate strength, MPa	600	192

The von Mises effective stress of the model under increasing compressive pressure (Figure 10b-c) indicated localized plasticity at the sphere interfaces, which led to sphere deformations. Simulated stress strain curve compared well with the experimental curve (see Figure 10d). The simulated curves became irregular at large strains because the implicit algorithm used in LS-DYNA struggled to converge because of the large number of contact surfaces. The simulated curve at 550 °C is noticeably higher than the experimental curve. This discrepancy is attributed to strengthening of the spherical shells due to oxidation of the steel foam at elevated temperatures (see Figure 9). This strengthening was not accounted for in the computational model.  
 315  
 320

The plastic strains localized in a few contact locations at 1.2 % global en-

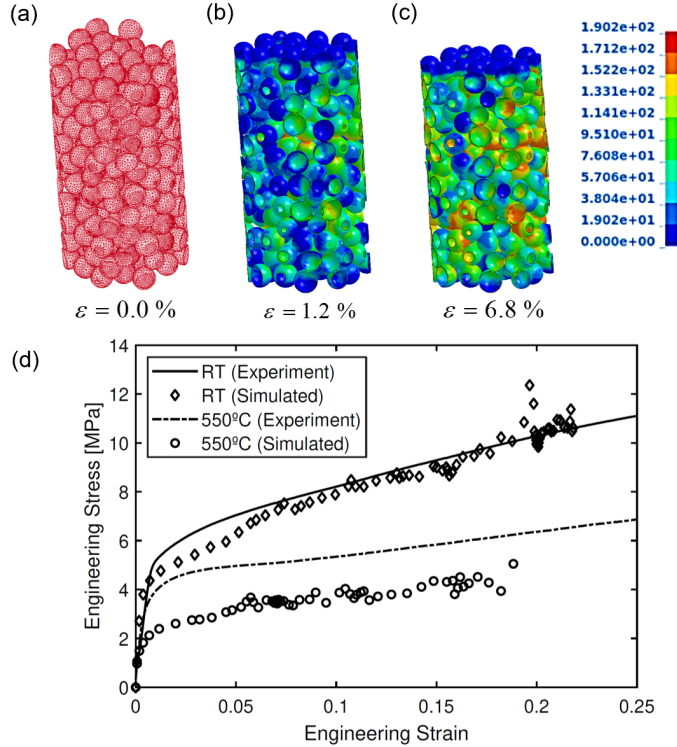


Figure 10: Comparison of computational (diamonds and circles) and experimental (continuous lines) strength predictions at room (RT) and high temperature ( $550^{\circ}\text{C}$ ). Von Mises stress (MPa) localized in the contact regions of the hollow steel spheres. Multiple and irregular load paths followed the random packing of the spheres, which resulted from the nature of the manufacturing process. Whereas simulated and experimental data showed good agreement, steel foam samples exhibited higher stiffness and strength at high temperatures when compared to the computational prediction.

gineering strain with progressively more localized plasticity regions with larger volume appearing at larger strains (Figure 11a-c). The randomness and tortuosity of the internal load paths is consistent with experimental study by Gründer et al. [? ]. They tracked increasing contact areas between the spheres using CT images, while increasing the compressive loads. The location of the contact areas and direction of the local load paths changed from sphere to sphere in a random, chaotic manner. It is consistent with our simulated cross-sections in the micro-model. Figure 11d-f illustrate the typical deformation mechanism of the individual spheres. Even though only cross-sections are shown, these deformations are 3-dimensional and mostly axi-symmetric. The key parameters identified by [? ], such as sphere radius  $R$ , thickness  $t$ , diameter of the contact area, and degraded mechanical properties of the base metal are all significant. The simulations showed that the diameter of the contact area was not constant; it gradually increased until the sphere collapsed at large strains. The simulations clearly indicated that plasticity dominated the local deformations of our HS steel foam samples.

#### *4.1. Insights from the analytical expressions for buckling of a spherical shell*

Pressure applied to a sphere,  $q_c$  needs to satisfy equilibrium with the membrane stress within the walls of the spherical shell [? ]:

$$\sigma_{shell} 2\pi R t = q_c \pi \frac{d_c^2}{4} \quad (3)$$

Thus, the membrane stress resulting from the applied pressure can be approximated as:

$$\sigma_{shell} = q_c \frac{d_c^2}{8Rt} \quad (4)$$

When the critical limit of the membrane stress is exceeded, it may fail either due to material yielding at the elastic limit,  $\sigma_y$ , or due to the buckling arising

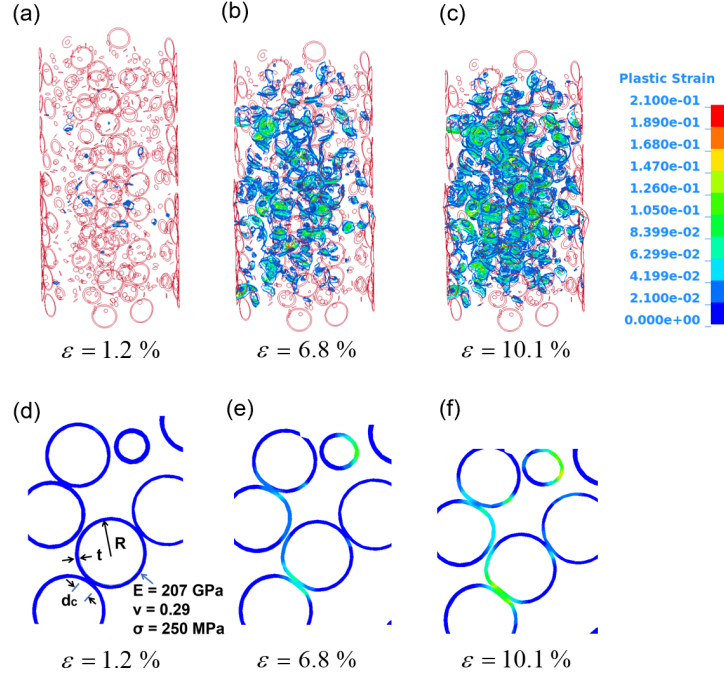


Figure 11: Plasticity localized at sphere interfaces experiencing plastic deformations arising from contact forces. As the load increased, the number of contact pairs and subsequently, plastic regions surged (b-c). Radius,  $R$  and thickness,  $t$  of the spherical shell, the diameter of the contact interface,  $d_c$  and material properties of the hollow spheres influence the local resistance mechanism (d). Following the initial yielding around the contact region, the plasticity spreads toward the equator of the sphere, accompanied by the gradually increasing diameter of the plastic hinge hoop moving outwards from the initial contact area (e-f). Due to the random packing, the number of contact regions and their directions vary from sphere to sphere, which is consistent with experimental study reported by Fallet et al. [? ].

from its geometric imperfections. The shell's stress limit to avoid the elastic buckling is taken from [? ] as:

$$\sigma_{cr} = \frac{Et}{R\sqrt{3(1-\nu^2)}} \quad (5)$$

Yielding typically leads to geometrical buckling anyway and the loss of the ideal spherical shape. Thus, the shell capacity of a hollow sphere can be expressed as:

$$\sigma_{failure} = \min(\sigma_y, \sigma_{cr}) \quad (6)$$

In the simulations, the steel base metal had a modulus of elasticity of  $E = 200$  GPa, Poisson's ratio of  $\nu = 0.29$ , and yield stress of  $\sigma_y = 250$  MPa. The average radius and thickness of the spheres were reported in a previous study [? ] as  $R = 1.86$  mm and  $t = 0.02$  mm, respectively. The resulting geometrical slenderness, expressed as the ratio of the radius to the thickness,  $R/t = 93$ , is consistent with the plastic buckling region (Figure 12a). A more general measure of the slenderness is the ratio of the plastic yield stress to the elastic buckling stress because it includes the influence of the material properties on the slenderness:

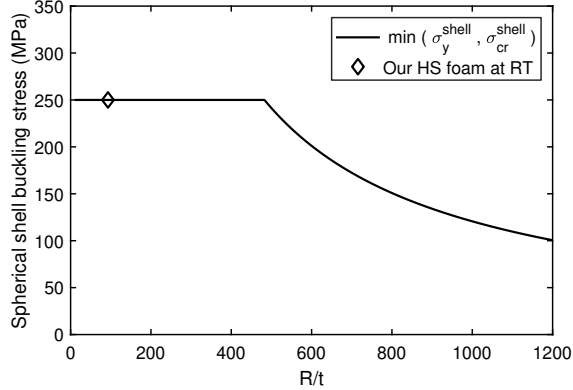
$$\lambda = \frac{\sigma_y}{\sigma_{cr}} \quad (7)$$

If slenderness  $\lambda < 1$ , then the structure is controlled by the material failure, namely plastic yielding. Alternatively,  $\lambda > 1$  indicates high slenderness and propensity for elastic buckling (Figure 12b). Winter [? ] developed an empirical curve for metallic plates, which showed that the transition between plastic and elastic buckling capacities is more gradual, and that there exists additional post-buckling reserve capacity in the elastic buckling regime. Even considering

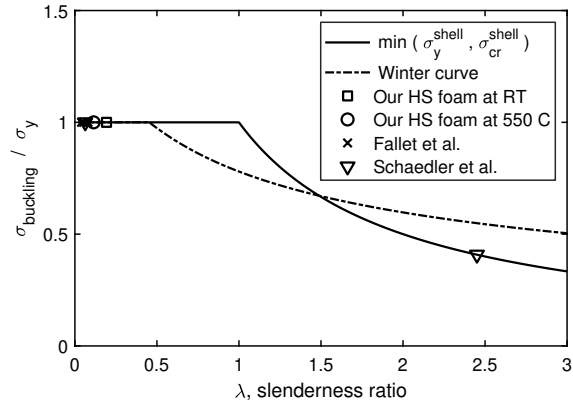
Winter's curve, the HS steel foam, as well as other foams reported by [? ], are  
370 still controlled by plastic buckling.

Coincidentally, the elastic buckling equations of a spherical shell also describes the elastic buckling capacity of a circular shell. Thus, the buckling curve in Figure 12b can also be used to analyzed hollow tubular lattice structures. Even considering the lightest metallic material achieved to-date by Schaedler  
375 et al. [? ], only one of their configurations was in the elastic buckling region. Schaedler's experiments showed that the slender lattice exhibited large, reversible deformations, while the stub lattices experienced non-reversible deformations but higher absolute strength. These experimental observations are consistent with plastic and elastic buckling of the cylindrical shells at the junctions of the hollow tubular struts.  
380

Based on a review of available data, conventionally produced HS foams exhibit local deformation mechanism controlled by the plastic buckling of the spherical shells. Thus, the thermal degradation of the global mechanical properties of our HS foam specimens is anticipated to be controlled by the influence  
385 of elevated temperatures on the base metal's yield stress.



(a) The effect of geometric slenderness on the buckling capacity of a single sphere.



(b) The effect of slenderness ratio on the buckling strength of a hollow sphere.

Figure 12: Buckling capacity of a single spherical shell expressed in terms of its critical membrane stress. Geometric slenderness of our hollow sphere steel foam expressed as the ratio of radius to thickness,  $R/t$  is low and consistent with the plastic buckling mechanism. Normalized theoretical buckling stress as a function of the non-dimensional slenderness parameter,  $\lambda$  overlaid with a range of theoretical capacities of foams and tubular lattice structures. Apart from the ultra-light metallic lattice, most of the manufactured cellular structures have very low slenderness, which is consistent with the irreversible, plastic buckling.

Regarding the influence of the temperature on the stiffness of the foam, radial displacement of a spherical shell under uniform external pressure,  $q$  is a function of its geometry and elastic constants [? ]:

$$w(\varphi) = \frac{q(1 + \nu)R^2}{Et} \left[ k(\varphi) \cot \varphi + \cos \varphi - \frac{1}{1 + \cos \varphi} \right] \quad (8)$$

<sup>390</sup> where  $k(\varphi)$  is the auxiliary variable:

$$k(\varphi) = \left( 1 - \frac{1}{1 + \cos \varphi} + \log(1 + \cos \varphi) \right) \sin \varphi \quad (9)$$

The deformation of the apex corresponds to  $\varphi = \frac{\pi}{2}$ , which gives:

$$w_{apex} = -\frac{q(1 + \nu)R^2}{Et} \quad (10)$$

<sup>395</sup> Since the direct influences of temperature on the radius and thickness of the sphere, as well as Poisson's ratio, are expected to be minimal, the thermal degradation of the foam stiffness is anticipated to be controlled by the base metal's modulus of elasticity.

## 5. Standard Metrics Calculated based on ISO Standard 13314:2011

<sup>400</sup> The following sections synthesize experimental observations to reveal the trends of the macroscopic material properties such as the plateau stress and ambient-temperature modulus of elasticity. Based on the computational and analytical considerations described in Section 3, it was anticipated that the phenomenological properties of the HS foam, with stub spherical shells, would primarily reflect the thermal degradation trends of their base metals' plastic properties.

### <sup>405</sup> 5.1. Yield Strength

Porous metallic materials are known to exhibit substantial plastic yielding capacity following an initial elastic phase, but they do not typically ex-

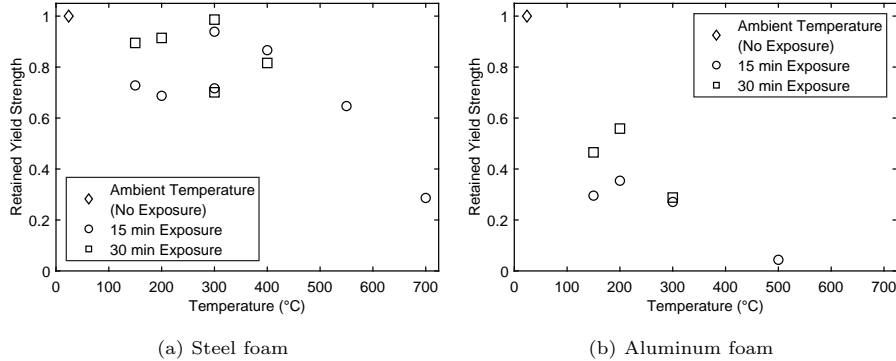


Figure 13: Retained yield strength  $\sigma_y/\sigma_{y,amb}$ , measured using the 0.2 % strain offset method, for: (a) HS steel foam, and (b) PM aluminum foam. In Equation (11),  $\sigma_y$  corresponds to the projection of the plastic modulus at zero strain.

hibit a “yield plateau”. Therefore, ISO Standard 13314:2011 recommends using the 0.2 % strain offset method to calculate the quasi-elastic compressive yield strength of porous metallic materials. Figure 13 show the retained yield strength of the HS steel and PM aluminum foams. At temperatures at or below 400 °C the HS steel foam retained an average of about 80 % of its ambient-temperature yield strength, but at temperatures exceeding 400 °C the yield strength was significantly degraded. The PM aluminum foam retained an average of less than 50 % of its ambient-temperature yield strength at or below 200 °C, and the retained yield strength was only 4.4 % at 500 °C.

### 5.2. Plateau Stress

The plateau stress, shown in Figure 14, was calculated following ISO Standard 13314:2011 as the average value of the stresses within the strain range spanning from 0.20 mm/mm and 0.30 mm/mm. There was little degradation in the measured plateau stress of the HS steel foam specimens at or below a 400 °C. However, the plateau stress of the PM aluminum foam specimens had significantly degraded by approximately 50 % at only 150 °C (i.e., at only 23 % of aluminum’s melting point).

The exposure (15 min or 30 min) had relatively little influence on the retained

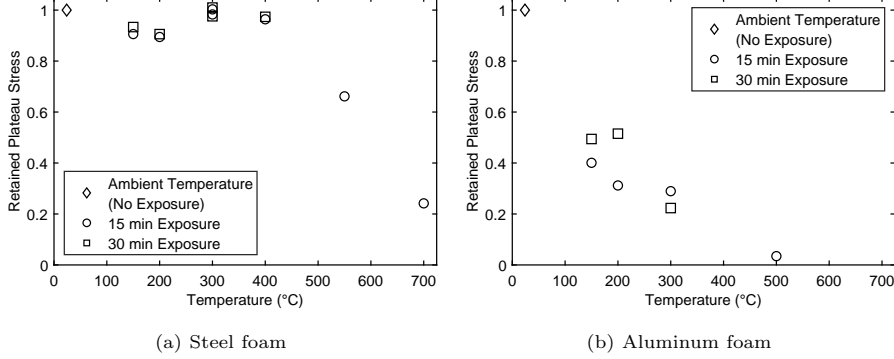


Figure 14: Retained plateau stress  $\sigma_{p1}/\sigma_{p1, \text{amb}}$ , where the plateau stress is depicted in Figure 7 as the average stress computed between 20 % and 30 % strain, for: (a) HS steel foam, and (b) PM aluminum foam.

plateau stress for the HS steel foam; the retained plateau stress for the two exposures did not differ by more than 4.0 %. The retained plateau stress of the PM aluminum foam was more scattered, but no systematic influence of exposure on the energy absorption capacity was observed. It was noted that the porosity of the PM aluminum foam specimens ranged from 71.4 % to 81.8 %, which may have increased the variability in their calculated mechanical properties, relative to those for the HS steel foam specimens.

### 5.3. Additional Metrics Calculated based on Multi-Parameter Curve Fit

To further characterize the response of the HS steel and aluminum foams,  
435 the nine-parameter phenomenological equation

$$\sigma(\varepsilon, T) = \begin{cases} \frac{(E_i(T) - E_p(T)\varepsilon)}{\left(1 + \left|\frac{(E_i(T) - E_p(T)\varepsilon)}{\sigma_y(T)}\right|^{n_y(T)}\right)^{\left(\frac{1}{n_y(T)}\right)}} + E_p(T)\varepsilon, & \varepsilon \leq \varepsilon_d \\ \sigma_d + \frac{(E_b(T) - E_d(T))(\varepsilon - \varepsilon_d(T))}{\left(1 + \left|\frac{(E_b(T) - E_d(T))(\varepsilon - \varepsilon_d(T))}{\sigma_p(T)}\right|^{n_b(T)}\right)^{\left(\frac{1}{n_b(T)}\right)}} + E_d(T)(\varepsilon - \varepsilon_d(T)), & \varepsilon > \varepsilon_d \end{cases} \quad (11)$$

where

$$\sigma_d(T) = \frac{(E_i(T) - E_p(T))\varepsilon_d(T)}{\left(1 + \left|\frac{(E_i(T) - E_p(T))\varepsilon_d(T)}{\sigma_p(T)}\right|^{n_y(T)}\right)^{\left(\frac{1}{n_y(T)}\right)}} + E_p(T)\varepsilon_d(T), \quad (12)$$

was fitted to the compressive stress-strain response of each specimen by minimizing the square area between the fitted curve and the experimental data. Similar five-parameter models have been successfully used in previous research  
440 to characterize the thermal-structural performance of structural components, such as high-strength bolts (see [? ]). Equation 11 is piecewise with the two curve segments joined at the densification point  $(\varepsilon_d, \sigma_d)$ , where  $\varepsilon_d$  is the densification strain and  $\sigma_d$  is the densification stress; each of the two segments is based on the nonlinear four-parameter “Richard Equation”, which was formulated in  
445 [? ]. The coordinates  $(\varepsilon_d, \sigma_d)$  also correspond to the inflection point defining the transition to stiffening (densification) behavior. In Equations 11 and 12,  $\sigma$  is the compressive stress,  $\varepsilon$  is the compressive strain, and  $E_i$  and  $E_p$  are initial elastic and plastic hardening modulus of the stress-strain response, respectively,  $\sigma_y$  is a reference load that corresponds to the projection of the plastic modulus  
450 at zero strain, and  $n_y$  is a shape parameter that controls the sharpness of the transition from the elastic stiffness to the plastic stiffness. The densification takeoff modulus  $E_b$  permits a different takeoff slope for densification than the plastic hardening modulus,  $\sigma_p$  is the projection of the densification stress at zero strain,  $n_d$  is a shape parameter controlling the sharpness of the transition from  
455 the plastic stiffness to the densification stiffness  $E_d$ , and  $(T)$  denotes dependence of the stiffness or capacity parameter on temperature.

The fitted values for the parameters in Equation 11 were determined using constrained gradient-based nonlinear multivariable optimization techniques available in MATLAB’s Optimization Toolbox ([? ]). Tables 3 and 4 (located  
460 in the appendix) presents a summary of the final fitted parameters for each individual foam specimen, and quality of the analytical fits is also shown in Figure 15. Discussion on each of the calculated parameters is provided in the

following sections.

### 5.3.1. Quasi-Elastic Modulus

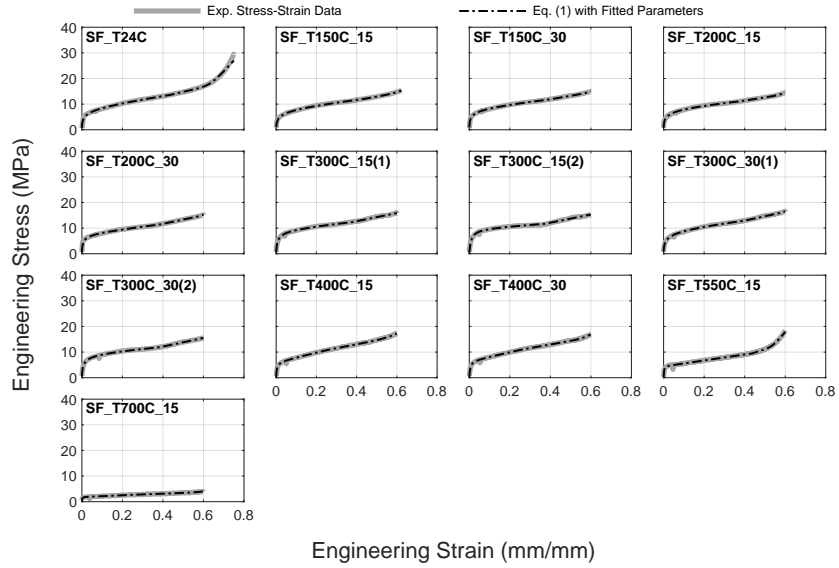
465 The quasi-elastic modulus is the initial slope of the elastic phase of the compressive stress-strain curve. It should be noted that the definition of the quasi-  
466 elastic modulus differs slightly from that of the elastic gradient, which can be calculated only after the specimen has been loaded and subsequently unloaded.  
467 The quasi-elastic modulus was calculated by fitting Equation 11 within  $[0, \varepsilon_y]$ ,  
468 where  $\varepsilon_y$  is the yield strain calculated using the 0.2 % offset method recommended by ISO Standard 13314:2011. Figures 16a and 16b show Equation 11,  
469 with fitted parameters calculated using structural optimization techniques, relative to the stress-strain data in the elastic phase. Obviously, Equation 11 can provide a very close approximation to the actual experimental data. The fitted  
470 parameter values for each specimen are provided in the appendix.

Figure 17 show the resulting retained quasi-elastic modulus as a function of temperature. While values for the retained quasi-elastic modulus of the HS steel foam were widely scattered, the quasi-elastic modulus did not degrade noticeably with increasing temperature (i.e., the value of the retained quasi-  
471 elastic modulus was greater than 1.0 across the entire temperature range). The largest increases in retained quasi-elastic modulus were at 200 °C and 300 °C. Conversely, quasi-elastic modulus of Aluminum foam deteriorated rapidly with the increase of the ambient temperature.

### 5.3.2. Quasi-Hardening Modulus

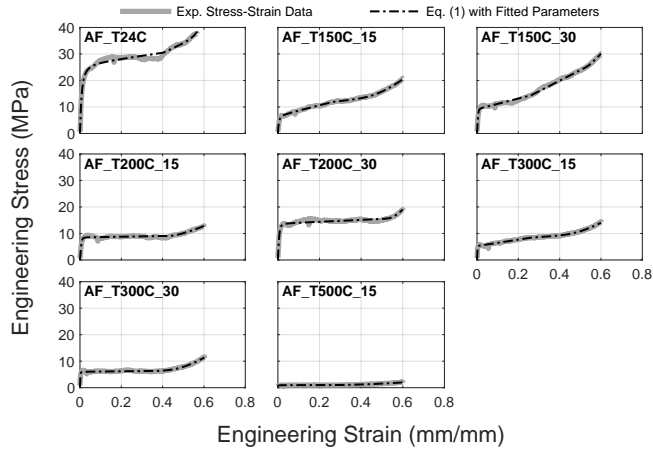
485 As described above, following yield closed-cell foams exhibit significant plastic hardening, which differs from the elastic-perfectly material behavior where the hardening modulus is assumed to be close to zero. To determine the quasi-hardening modulus, Equation 11 was fitted using global error minimization techniques to the entire experimental stress-strain curve for each specimen (shown  
486 in Figure 15).

490 The fitted parameters enable close approximation of the full stress-strain



Engineering Stress (MPa)

(a) Steel foam



Engineering Stress (MPa)

(b) Aluminum foam

Figure 15: Equation (9) fitted to the full stress-strain behavior of each specimen for: (a) HS steel foam specimens, and (b) PM aluminum foam specimens. Each plot is denoted by specimen name, using an annotation located in the upper-left-hand corner.

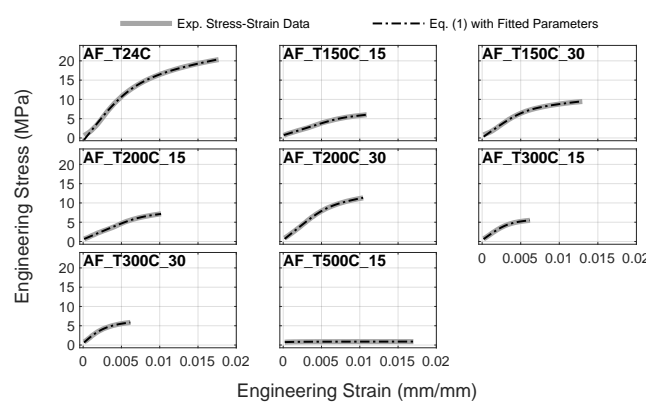
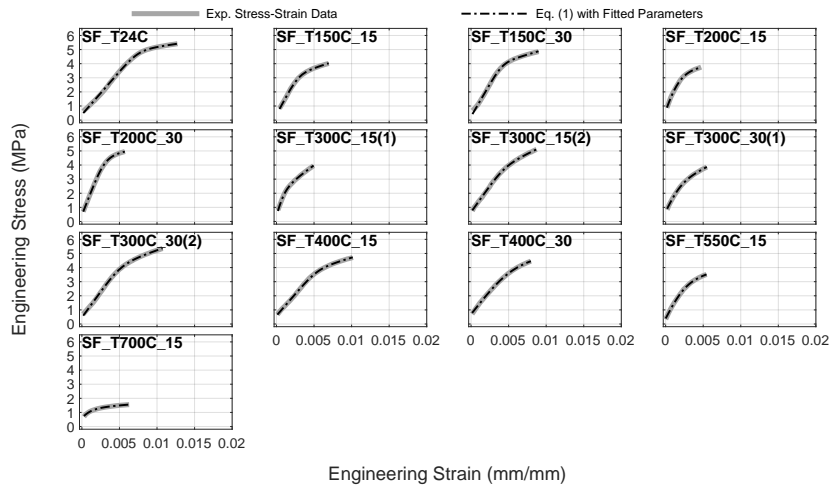


Figure 16: Equation (9) fitted to the initial strain range of the stress strain curve for: (a) HS steel foam specimens, and (b) PM aluminum foam specimens. Each plot is denoted by specimen name, using an annotation located in the upper-left-hand corner.

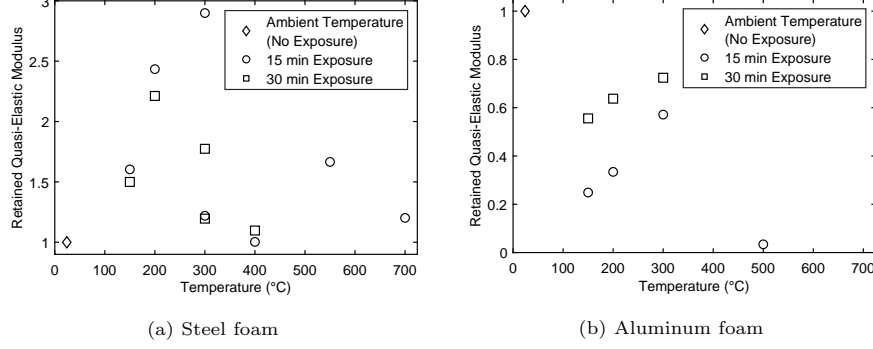


Figure 17: Retained quasi-elastic modulus  $E_i/E_{i,amb}$ , determined by fitting Equation (9) to the initial strain range of the stress strain curve for: (a) HS steel foam specimens, and (b) PM aluminum foam specimens.

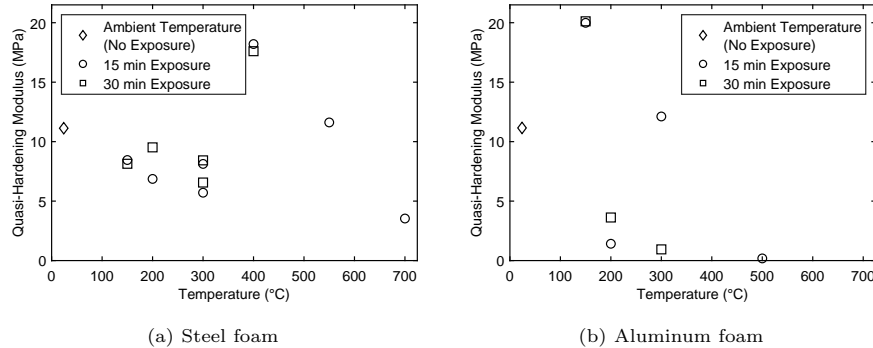


Figure 18: Quasi-hardening modulus, defined by plastic stiffness  $E_p$ , for: (a) HS steel foam, and (b) PM aluminum foam.

behavior of both HS steel and PM aluminum foams even throughout the densification phase. Table 4, located in the appendix, presents a summary of the fitted parameter values for each individual specimen. Figure 18 shows the resulting values of the quasi-hardening modulus as a function of temperature.  
495

### 5.3.3. Densification Strain

The point of intersection of the two piecewise curves in Equation 11 identically defines the inflection point between those segments. The strain location of this inflection point is designated in this study as the densification strain, or the strain at which the tangent slope of the stress-strain curve begins to increase rel-  
500

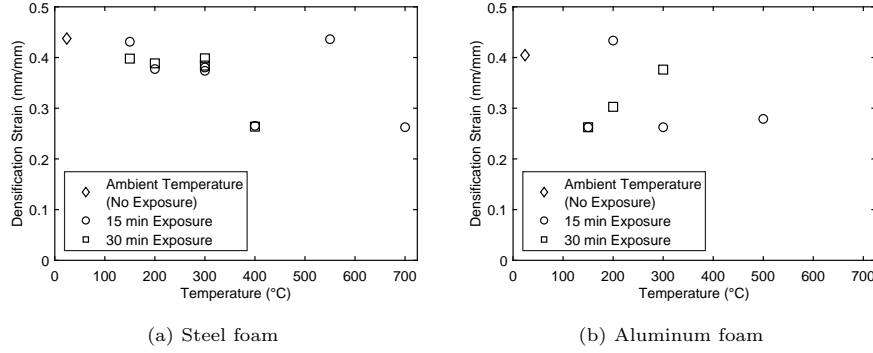


Figure 19: Densification strain, defined at the point of intersection of the two piecewise curves in Equation 11, which identically defines the inflection point between those segments, for: (a) HS steel foam, and (b) PM aluminum foam.

ative to the hardening modulus thereby indicating densification of the metallic foam. Figure 19 does not show a clear influence of either elevated temperatures nor exposure on the densification strain. Overall for both the HS steel and PM aluminum foams, the densification strain is scattered by approximately 0.08 mm/mm about a mean densification strain value of about 0.35 mm/mm.  
505

#### 5.3.4. Energy Absorption Efficiency

While ISO Standard 13314:2011 does specify a methodology for calculating the energy absorption efficiency, this methodology first requires characterization of the densification strain which could only be reliably determined using 510 the multi-parameter optimization approach described above. The energy absorption efficiency is calculated per ISO Standard 13314:2011 as the ratio of energy absorption capacity to the product of the maximum compressive stress (within the strain range spanning from 0.00 mm/mm to the densification strain), and the value of the densification strain (see Figure 20). The energy absorption 515 capacity is shown as the hatched area in Figure 20, and the product of the maximum compressive stress within the strain range and the densification strain is the area bounded by the blue rectangle.

The energy absorption capacity is calculated either by integrating the stress-strain curve between strains of 0.00 mm/mm and 0.50 mm/mm, or by multi-

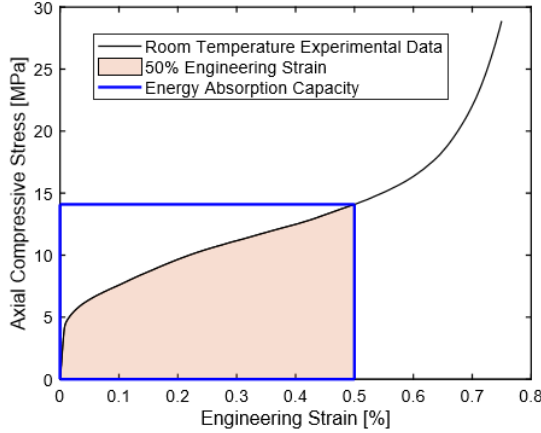


Figure 20: Schematic representation of methodology for calculating energy absorption efficiency.

plying the plateau stress by 1.3. The integration-based approach was used in this study. As expected, trends in the behavior of the energy absorption capacity are similar to those of the plateau stress. Interesting, while the energy absorption capacity degrades more quickly with increasing temperature for the PM aluminum foam than for the HS steel foam, the energy absorption capacity of the two types of metallic foams is similar between temperatures of 150 °C and 300 °C (Figure 21). The exposure had relatively little influence on the energy absorption capacity for the HS steel foam; the energy absorption capacity for the two exposures did not differ by more than 4.0 %. The energy absorption capacity of the PM aluminum foam was more scattered, but no systematic influence of exposure on the energy absorption capacity was observed.

For the HS steel foam specimens, the energy absorption efficiency is nearly constant across all tested temperatures at a value of approximately 78 %, and irrespective of the exposure (Figure 22). This trend implies that the shapes of the stress-strain curves are self-similar (at least up to the densification strain) and could be reproduced, in an approximate sense, by scaling the ambient temperature stress-strain response by a temperature dependent scalar reduction factor. Conversely, for the aluminum foam specimens, their small values of the harden-

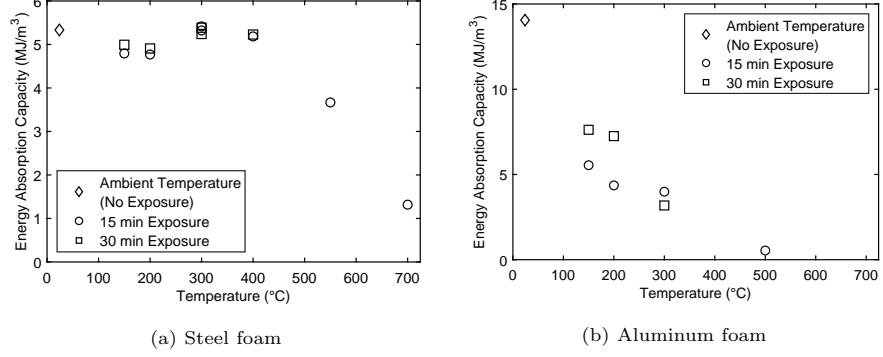


Figure 21: Energy absorption capacity, calculated by integrating the stress-strain curves of the steel foam specimens between strains of 0.00 and 0.50, for: (a) HS steel foam, and (b) PM aluminum foam.

ing modulus at higher temperatures indicates that their behavior approaches an elastic perfectly plastic state, which contributed to their larger values of energy absorption efficiency.

540

## 6. Discussion

The computational analyses revealed that the local capacity at the spherical shell length-scale, following initially elastic deformations, was controlled by the plastic buckling, mutual indentation, and bending of the spherical shells in contact. These contact regions are distributed randomly throughout the sample, resulting in localized plasticity. The deformation of the spheres is driven by bending of a spherical region, which increases radially as the material globally hardens. Random load paths complicate the development of closed-form multi-scale models linking local sphere geometry with the global macroscopic foam strength. Our computational observations compliment experimental studies by Gründer [? ] and by Fallet et al. [? ], which also used CT-images to investigate internal foam deformations. Fallet proposed using the Weibull distribution to estimate the expected number of contact regions as a function of the overall global strain. Further work is needed to enable analytical predictions of the macroscopic foam properties from the geometry of the hollow spheres and their

545

550

555

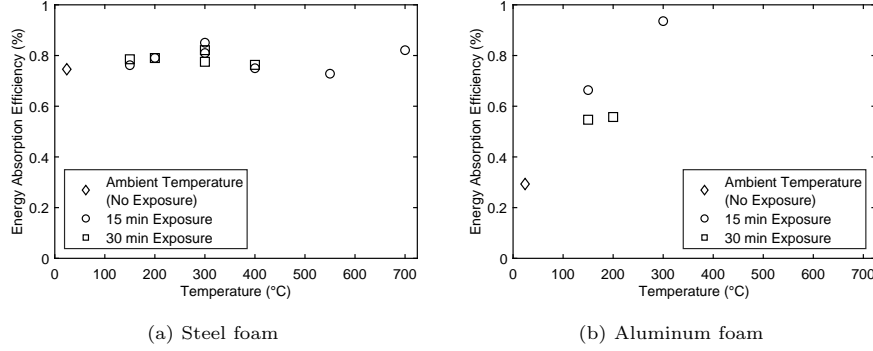


Figure 22: Energy absorption efficiency, calculated per ISO Standard 13314-2011 as the ratio of energy absorption capacity to the product of the maximum compressive stress (within the strain range spanning from 0.00 mm/mm to the densification strain).

base metal properties through the use of statistics and elasto-plastic analytical modeling of the capacity of a spherical shell. Nevertheless, our simulations also indicated that the use of random variables for the sphere location and in the consideration of the packing pattern is necessary.

As expected from the fundamental buckling analysis of spherical shells, the thermal degradation of the metallic foams generally followed the temperature-induced reduction of yield stress of their respective base metals. Figure 23 compares the retention factors found in Eurocode ([? ]) for the solid, bulk steel and aluminum to the thermal degradation rate of the metal foams. The data for the HS steel foam followed the trends of the base metal with reasonable consistency. Note that Eurocode does not specify a specific time of exposure, but only states that the heating rate stay between 2 °C/min to 50 °C/min. Thus, it refers to the continuous exposure to the given temperatures. The testing conducted in this study did not show a significant influence of thermal exposure time (15 min or 30 min) on the thermal-mechanical properties of either the HS steel or PM aluminum foams.

According to EN 1999-1-2 [? ], the mechanical properties of solid aluminum degrade at much lower temperatures than those of solid steel. Taherishargh et al. [? ] previously reported that the reduction in material properties of foams fol-

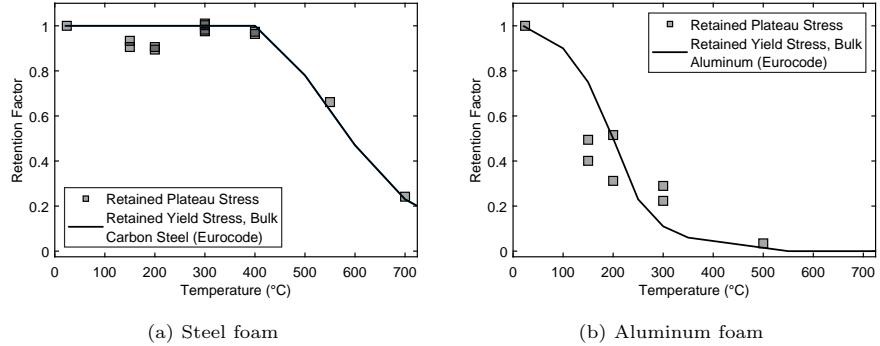


Figure 23: Comparison between retention factors for (a) HS steel foam with those for carbon steel in [? ], and (b) PM aluminum foam with those for aluminum in [? ].

575 low the trend of the solid material. The yield stress of solid aluminum decreases  
 580 by about 20 % at 150 °C and about 90 % at 300 °C; the results for the PM aluminum foam followed a similar trend, but with even more significant reductions  
 in strength (more than 50 % at 150 °C for some specimens, see Figure 23). The  
 585 mechanical performance of the PM aluminum foam was essentially negligible at  
 temperatures exceeding 300 °C. These findings about aluminum foam behavior  
 at elevated temperatures (compressive strength, energy absorption capacity and  
 elastic modulus) are consistent with previous studies of aluminum foams in the  
 literature ([? ], [? ], [? ]), and for the HS steel foams by [? ].

590 Although manufacturing of steel foam is more expensive than aluminum  
 595 foam due to increased energy costs deriving from the higher melting point of  
 steel, the retained strength and stiffness of HS steel foam at a given elevated tem-  
 peratures is clearly larger than that of the PM aluminum foam. The Iron (Fe)  
 based HS steel foam showed only minor degradation in mechanical performance  
 at temperatures less than 400 °C, and retained 60 % of its compressive strength  
 600 at 550 °C. Such resilience might allow steel foam components to perform their  
 intended functions even under elevated temperatures, by largely retaining the  
 safety factors embedded in typical designs.

605 The formation of a blue oxide surface skin during heating of HS steel foam  
 specimens (see Figure 9) increased its stiffness within the temperature range of

595 200 °C and 300 °C. These findings are consistent with Bekoz et al. [? ], who  
reported an increase in compressive yield strength and stiffness for PM steel  
foams for temperatures up to 400 °C, and a decrease above that temperature.  
Bekoz et al. [? ] suggested an aging effect (dynamic age-hardening) as the  
reason for the increase in mechanical properties up to 400 °C but did not detect  
600 any enhancement in the compressive strength over the temperature range.

Considering the large surface areas of metallic foams, surface-oxidizing chem-  
ical reactions could have a significant positive influence on the thermal-mechanical  
performance of steel foams. For example, pre-oxidization of FeCrAl enhances  
its mechanical properties at temperatures up to 400 °C. The potential for such  
605 reactions to reliably increase thermo-mechanical performance should be also in-  
vestigated for other base metals and alloys because these reactions could allow  
metallic cellular structures to outperform their constituent base metals.

## 7. Summary and Conclusions

The compressive behavior of hollow sphere (HS) steel foam and powder met-  
610 allurgy (PM) aluminum foams were studied at elevated temperatures to char-  
acterize their thermo-mechanical properties. The experimental results showed  
that the HS steel foam retained more than 89 % of its compressive strength,  
when measured by the plateau stress, up to 400 °C, and 69 % of its strength  
and energy absorption capacity at 550 °C. At 700 °C, much of the structural  
615 integrity of the HS steel foam was largely diminished, retaining only 24 % of  
its compressive strength and energy absorption capacity. Contrarily, the PM  
aluminum foam retained only about 45 % of its strength and energy absorption  
capacity at 150 °C, and had virtually no strength (only 3.5 %) remaining at  
500 °C.

620 High-resolution computational models showed that, under increased defor-  
mation, plasticity spreads toward the equators of individual hollow spheres,  
gradually increasing the diameter of their plastic hinge hoops until buckling of  
the sphere-walls occurred. This observation was further supported by analyti-

cal consideration of buckling of a spherical shell. Thus, the local plasticity and  
625 plastic stress are critical for the thermal deterioration of metallic foams' mechanical capacities because they control local plastic buckling. As anticipated from the simulations, the retained plateau stress for both the HS steel and PM aluminum foams generally followed the elevated-temperature degradation of the yield stress of their respective base metals (available from Eurocode EN  
630 1993-1-2:2005 and EN 1999-1-2:2007). However, based on the general buckling stability considerations, it might be possible to manufacture ultra-thin-walled foams, which should exhibit highly elastic, reversible deformations. Their thermal behavior would be expected to follow thermal deterioration of modulus of elasticity of the base material. This observation is consistent with previously  
635 reported hyper elastic behavior of ultra-thin-walled hollow lattice structures [? ].

The experiments also revealed an interesting chemical phenomenon. A blue oxide film formed on the surface of the steel foam. This film was likely responsible for the moderate increases of quasi-elastic gradient between temperatures of  
640 200 °C, 300 °C, higher stress-strain curves in the range of 300 °C to 400 °C then 100 °C as well as discrepancy between the simulated and experimental stress strain curves of HS steel foam at higher temperatures. Chemical reactions that occur at elevated temperatures will be considered in future studies because they might allow metallic foams to exceed thermo-mechanical performance of their  
645 base metals by taking advantage of the large surface area to volume ratio in cellular structures.

The high thermal resilience of steel foams suggests that their potential range of application might extend to temperatures traditionally precluded for polymeric or even aluminum foams. The energy absorption capacity of the HS steel foam was nearly constant at the temperatures below 400 °C, and significant residual energy absorption capacity (about 69 %) remained at 550 °C. In addition, the energy absorption efficiency was essentially constant at about 80 % and did not diminish at elevated temperatures. Thus, steel foams may be suitable for dissipation of impacts, crashes or other extreme loads at elevated temperatures.  
650

655 The crashworthiness could be combined with heat exchange functions in open cell foams. This research is a part of broader effort to develop understanding of cellular metallic materials with relevance to aerospace, automotive, energy and infrastructure applications.

### List of Acronyms

HS	Hollow Sphere
PM	Powder Metallurgy
ISO	International Organization for Standardization
IFAM	Fraunhofer Institute for Manufacturing Technology and Advanced Materials
MTS	Material Testing System
UTM	Universal Testing Machine
RCP	Random close-packed
RT	Room Temperature
SF	Steel Foam
AF	Aluminum Foam
METFOAM	International Conference on Porous Metals and Metallic Foams
EPSRC	Engineering and Physical Science Council

### List of Symbols

660	$\alpha$	Correction factor used for the measurement of the spherical pore size
	$\lambda$	Slenderness
	$\nu$	Poisson ratio
	$\omega_{apex}$	Deformation of the sphere apex under uniform pressure
	$\sigma_{failure}$	Failure stress
665	$\sigma_{cr}$	Critical limit of membrane stress
	$\sigma_{cr}^{shell}$	Critical stress of the spherical shell

$\sigma_d$	Densification Stress that define the transition to stiffening behavior
$\sigma_{pl}$	Plateau Stress
$\sigma_p(T)$	Projection of densification stress at zero strain
$\sigma_{shell}$	Buckling Stress of Spherical Shell
$\sigma_y$	Yield stress
$\sigma_y^{shell}$	Yield stress of the spherical shell
$\varepsilon$	Compressive strain
$\varepsilon_d$	Densification Strain that define the transition to stiffening behavior
$\varepsilon_d(T)$	Densification stiffness
$\varepsilon_y$	Yield strain calculated using the 0.2 % offset method
$\varphi$	Polar coordinate, where 0 corresponds to the equator and $\pi/2$ to the apex of the sphere
$d_c$	Diameter of the contact area between the spheres
$E$	Young Modulus
$E_b(T)$	Slope of the segment, which constraints Richard's equation fit at the densification point $(\epsilon_d, \sigma_d)$ , which is obtained by minimizing the square area between the fitted curve and the experimental data
$E_d(T)$	Densification stiffness
$E_i$	Initial elastic modulus
$E_i(T)$	Initial elastic modulus at high temperature
$E_p$	Plastic hardening modulus
$E_p(T)$	Plastic hardening modulus at high temperature
$f_y$	Yield stress calculated using the 0.2 % offset strain method

690	$h_{proj}^i$	Height of the random cut plane used for measurement of the spherical pore size
	$n_b(T)$	Shape parameter that controls the sharpness of the transition from the plastic stiffness to the densification stiffness at high temperature, Figure 7
695	$n_y$	Shape parameter that controls the sharpness of the transition from the elastic stiffness to the plastic stiffness
	$n_y(T)$	Shape parameter that controls the sharpness of the transition from the elastic stiffness to the plastic stiffness at high temperature
	$q_c$	Pressure applied to a sphere
700	$R$	Sphere radius
	$r_{proj}^i$	Projected Radius used for measuring the size of the spherical pore
	$r_{true}$	True Radius of the spherical pore size
	$T$	Temperature
	$t$	Sphere Thickness
705	$q$	Applied pressure

### Acknowledgements

The authors would like to express heartfelt gratitude to our academic colleagues for their feedback and fruitful discussions. We are grateful to Fraunhofer IWU in Chemnitz and Fraunhofer IFAM in Dresden for the ongoing collaboration, and for their help with supplying the metallic foam rectangular prisms for mechanical testing. We would like to thank Dr Rene Vogel, Dr Thomas Hipke, Dr Olaf Andersen, Dr Peter Quadbeck and Dr Christian Hannemann.

We also would like to express our gratitude to technicians who assisted us during the mechanical tests, namely Mr Peter Heynes and David Jesson. We

<sup>715</sup> are also indebted to LS-DYNA support and developers for their assistance with the implicit, large deformation and large-strain micro-model.

This study was funded by the Research Framework of the European Commission under METFOAM Career Integration Grant 631827 with support from program manager Dr. Ing. Antonio Cipollaro. The work was also supported <sup>720</sup> by the impact acceleration grant no EP/P511456/1, provided by the Engineering and Physical Science Council (EPSRC) in the UK. Support of Dr. Sue Angulatta, a local program manager, is genuinely appreciated. Any opinions, findings, and conclusions expressed in this article are those of the author(s) and do not necessarily reflect the views of EPSRC or the European Commission.

<sup>725</sup> **Data availability**

The data is available upon request from the corresponding author.

## Appendix

### *Fitted Richard Equation Parameters*

The Richard Equation parameter values fitted only to elastic phase of each <sup>730</sup> specimen's stress-strain response are presented in Table 3, and the Richard Equation parameter values fitted to each specimen's full stress-strain curve are presented in Table 4.

Table 3: Richard Equation Parameters fitted only to Elastic Phase of Specimen Stress-Strain Curve.

Spec.	$E_i(T)$	$E_p(T)$	$\sigma_y(T)$	$n_y(T)$	$E_b(T)$	$E_d(T)$	$\sigma_p(T)$	$n_d(T)$	$(\varepsilon_d, \sigma_d)$
SF_T24C	611	76.9	4.4	10.01	-	-	-	-	-
SF_T150C_15	979	166.8	2.8	5.59	-	-	-	-	-
SF_T150C_30	916	156.5	3.4	7.71	-	-	-	-	-
SF_T200C_15	1487	3.7	4	2.39	-	-	-	-	-
SF_T200C_30	1351	84.8	4.5	4.98	-	-	-	-	-
SF_T300C_15(1)	1770	381	2	2.79	-	-	-	-	-
SF_T300C_15(2)	745	246.1	2.8	5.9	-	-	-	-	-
SF_T300C_30(1)	1084	238	2.5	3	-	-	-	-	-
SF_T300C_30(2)	730	183.1	3.3	6.19	-	-	-	-	-
SF_T400C_15	613	157.4	3	7.6	-	-	-	-	-
SF_T400C_30	670	58.9	4.4	3.43	-	-	-	-	-
SF_T550C_15	1017	78.8	3.4	2.6	-	-	-	-	-
SF_T700C_15	734	35.9	1.3	2.3	-	-	-	-	-
AF_24C	2514	327.2	15.2	2.62	-	-	-	-	-
AF_T150C_15	625	205.9	3.6	9.12	-	-	-	-	-
AF_T150C_30	1397	204.1	6.9	3.88	-	-	-	-	-
AF_T200C_15	840	166.9	5.5	6.21	-	-	-	-	-
AF_T200C_30	1602	347.4	7.7	4.81	-	-	-	-	-
AF_T300C_15	1437	85.6	5.1	3.5	-	-	-	-	-
AF_T300C_30	1820	48	6.2	2.2	-	-	-	-	-
AF_T500C_15	86	2.2	0.8	9.54	-	-	-	-	-

Table 4: Richard Equation Parameters fitted to Specimen Full Stress-Strain Curve.

Spec.	$E_i(T)$	$E_p(T)$	$\sigma_y(T)$	$n_y(T)$	$E_b(T)$	$E_d(T)$	$\sigma_p(T)$	$n_d(T)$	$(\varepsilon_d, \sigma_d)$
SF_T24C	15697	11.1	11.8	0.35	0.44	18.7	84.6	13.1	9.36
SF_T150C_15	12219	8.5	11.5	0.35	0.43	13.7	54	9.3	3.98
SF_T150C_30	22337	8.1	11.2	0.35	0.4	13.6	50.9	8.2	8.32
SF_T200C_15	15550	6.9	11.8	0.34	0.38	12.3	44.1	6.8	9.14
SF_T200C_30	3841	9.5	8.4	0.6	0.39	16.5	64.8	10.8	15.15
SF_T300C_15(1)	3322	8.1	10.2	0.6	0.38	15.9	43.9	11.7	100.28
SF_T300C_15(2)	1146	5.7	9.8	0.99	0.37	15.9	66.8	12.1	107.82
SF_T300C_30(1)	14081	8.4	13.3	0.35	0.4	17.1	63.3	9.6	20.33
SF_T300C_30(2)	3798	6.6	10.5	0.56	0.38	16.7	66.4	10.9	38.01
SF_T400C_15	2554	18.2	6.3	0.84	0.27	15.1	51.8	12.3	6.61
SF_T400C_30	1252	17.6	6.5	1.17	0.26	14	45.5	9.7	12.37
SF_T550C_15	1191	11.6	4.4	1.83	0.44	25	101.9	8.5	5.5
SF_T700C_15	649	3.5	1.8	1.63	0.26	2.9	12.3	3.1	8.03
AF_24C	2565	11.2	26.1	1.44	0.4	37.2	199.6	29.6	5.77
AF_T150C_15	1195	20	6.7	1.58	0.26	9.2	62.7	13.6	3.81
AF_T150C_30	1393	20.1	9.2	3.65	0.26	39.8	75.8	10	39.83
AF_T200C_15	961	1.4	8.5	3.39	0.43	2.9	43.8	11.3	0.79
AF_T200C_30	1694	3.6	13.7	2.4	0.3	3.6	67.6	15.9	20.5
AF_T300C_15	1666	12.1	5.3	3.93	0.26	5.5	45.9	10.6	4.18
AF_T300C_30	2165	0.9	6	2.68	0.38	3.7	59.4	11.8	1.86
AF_T500C_15	3774	0.2	1	0.78	0.28	0.7	6.8	2.2	1.3